

Collimated prompt gamma TOF measurements with multi-slit multi-detector configurations

**J. Krimmer^{a,*}, M. Chevallier^a, J. Constanzo^a, D. Dauvergne^a, M. De Rydt^{a,b},
G. Dedes^a, N. Freud^c, P. Henriquet^a, C. La Tessa^d, J.M. Létang^c, R. Pleskač^d,
M. Pinto^a, C. Ray^a, V. Reithinger^a, M.H. Richard^{a,c}, I. Rinaldi^e, F. Roellinghoff^{a,c},
C. Schuy^d, E. Testa^a, M. Testa^a, M. Vanstalle^d**

a

*Institut de Physique Nucléaire de Lyon; Université de Lyon, F-69003 Villeurbanne, France;
IN2P3/CNRS, UMR 5822; Université de Lyon 1, F-69622 Villeurbanne, France*

b

Instituut voor Kern- en Stralingsfysica, K.U.Leuven, Celestijnenlaan 200D, B-3001 Leuven

c

Université de Lyon, CREATIS; CNRS UMR 5220; Inserm U 1044; INSA-Lyon; Université Lyon 1; Centre Léon Bérard, Lyon, France

d

GSI Helmholtz Center for Heavy Ion Research, Planckstrasse 1, D-64291 Darmstadt, Germany

e

Heidelberg Ion Therapy Center and Department of Radiation Oncology, Im Neuenheimer Feld 450, 69120 Heidelberg, Germany

E-mail: j.krimmer@ipnl.in2p3.fr

ABSTRACT: Longitudinal prompt-gamma ray profiles have been measured with a multi-slit multi-detector configuration at a 75 MeV/u ^{13}C beam and with a polymethyl-methacrylate target. Selections in time-of-flight and energy have been applied in order to discriminate prompt-gamma rays produced in the target from background events. The ion ranges which have been extracted from each individual detector module agree amongst each other and are consistent with theoretical expectations. In a separate dedicated experiment with 200 MeV/u ^{12}C ions the fraction of inter-detector scattering has been determined to be less than 3 %. At the same experiment different collimator configurations have been tested and the shielding properties of tungsten and lead for prompt gamma rays have been measured.

KEYWORDS: Instrumentation for hadron therapy, prompt-gamma, 87.56.Fc, 87.53.Bn, 29.40.Mc.

Contents

1. Introduction	1
2. Multi-slit experiment at GANIL	2
2.1 Experimental setup	2
2.2 Data analysis	4
2.3 Results	5
3. Collimator test experiment at GSI	7
3.1 Experimental setup	7
3.2 Data analysis	8
3.3 Results	10
4. Conclusions	14

1. Introduction

The treatment of tumors via protons or carbon ions (hadrontherapy) is an emerging technique which benefits from the fact that ions deposit a large quantity of their energy close to the end of their path in the Bragg peak. This property, compared to conventional radiotherapy with X-rays, allows a maximization of the dose applied to the tumor and a minimization of the dose deposited in healthy tissues. Another advantage, in the case of carbon ions, is the higher relative biological effectiveness compared to photons, due to the higher ionization density.

Due to its sharp fall-off, a major issue for quality control during treatment with ion beams is the control of the Bragg peak position and its conformation to the tumor volume. A mismatch would lead to an over-dosage in healthy tissue and an under-dosage in the target volume.

Most of the methods which are investigated for an *in vivo* monitoring of the ion range during treatment are based on the detection of secondary radiation, as no primary radiation escapes from the patient. Several types of radiation have been considered for this purpose: anti-collinear 511 keV photons following a β^+ -decay, secondary protons from fragmentation processes (in the case of carbon ions), and prompt gammas generated at the decay of excited fragments.

The detection of 511 keV photons [1] via positron emission tomography (PET) has already proven its applicability in hadrontherapy (see e.g [2, 3]). However, when deducing the absorbed dose from the measured activity, biological wash-out needs to be taken into account. This is caused by long acquisition times which are required due to the limited number of produced β^+ emitters, since PET acquisition is hindered during beam delivery.

*Corresponding author.

Secondary protons following fragmentation processes can be detected in the case of carbon ion beams. The concept is to reconstruct the trajectories of the emitted particles and to extrapolate them to their point of creation (vertex) [4]. This proton interaction vertex imaging (PIVI) modality is studied by several groups [5, 6, 7].

Prompt gamma rays in the energy range up to 10 MeV are emitted nearly instantaneously after inelastic nuclear reactions of the incident ions. It has been shown that the production rate of these prompt gamma rays is highly correlated to the dose deposited by the primary particles [8, 9, 10], i.e. the Bragg peak position can be determined via a detection of the fall-off in the prompt gamma production rate. Systems following this approach comprise collimated cameras (both knife-edge [11, 12] and multi-slit cameras [13, 14]), as well as Compton cameras [15, 16, 17, 18, 19, 20]. It has recently been shown, that with the collimated camera concept ion ranges in homogeneous targets can be monitored with millimetric precision for a single spot in proton pencil beam scanning [21, 12]. Time of flight can be used to improve the signal to background ratio, as it helps eliminating uncorrelated signals induced by neutrons and scattered particles [10, 13, 21]. This is particularly necessary for carbon ion beams. Furthermore, it is also possible to detect density variations along the ion path [22].

The collimated camera has the advantage that no reconstruction is necessary, i.e. with a multi-slit multi-detector configuration a real-time monitoring of the ion range is possible. The question of the operability of such a configuration is raised, as high energy gamma scattering between adjacent detectors would dilute the position information and therefore the information about the ion range. The present article addresses this open question from the experimental side, with a comparison to simulations at the end. In a first experiment, measurements have been performed with a multi-slit multi-detector setup demonstrating the proof of principle. In a second step, in a separate experiment, the inter-detector scattering has been quantified. Furthermore, the influence of different collimator configurations, as well as different shieldings has been measured and results have been compared to Geant4 simulations. These activities are an intermediate step towards a real-size prototype. The obtained data serve also as an assessment of the accuracy of the Monte Carlo simulations which are used for an optimization of the collimator dimensions.

2. Multi-slit experiment at GANIL

2.1 Experimental setup

The measurement with a multi-slit multi-detector setup was performed at GANIL (Caen, France) with 75 MeV/u ^{13}C -ions. A top-view of the experiment is given in Fig 1. Four LYSO scintillation detectors were placed at 90° with respect to the beam axis behind a tungsten collimator with equidistant slits. A 5th LYSO detector was located behind a lead collimator under 90° at the other side of the beam axis (see Fig. 1 for the dimensions). The four LYSO detectors behind the multi-slit collimator have been arranged in a way as indicated in Fig. 2. The LYSO crystals were coupled via lightguides to photomultiplier (PM) tubes. Symmetric and asymmetric lightguides have been combined in a way to assure a close alignment of the crystals without being hindered by the size of the PM tubes. The properties of the LYSO detectors including their crystal type and size, as well as the type of used lightguides, are denoted in Tab. 1.

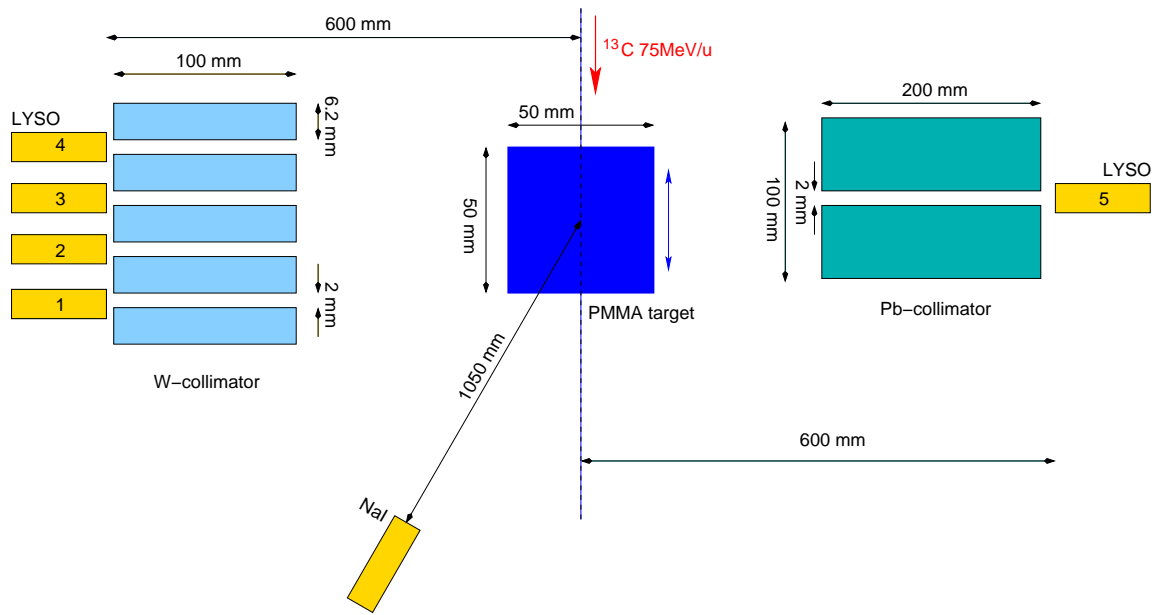


Figure 1. A multi-slit multi-detector configuration for measuring prompt gamma profiles at GANIL with 75 MeV/u ^{13}C -ions. The NaI-detector was placed underneath the target at 90° with respect to the beam direction. It is represented downstream to the target for the purpose of clarity. The figure is not to scale.

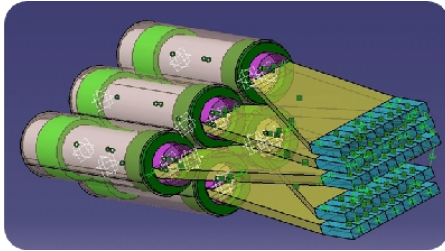


Figure 2. Indication of the arrangement of the LYSO detectors (here represented as pixellated arrays and with five detectors) behind the multi-slit collimator. A combination of symmetric and asymmetric lightguides assured a close placement of the scintillator crystals without being hindered by the size of the PM tubes.

Nr	1	2	3	4	5	6
type	pixel	mono	pixel	mono	mono	mono
size [mm^3]	$4 \times 40 \times 22$	$5 \times 40 \times 50$	$4 \times 40 \times 22$	$3 \times 40 \times 50$	$5 \times 40 \times 50$	$3 \times 40 \times 50$
lightguide	sym	asy	asy	asy	sym	sym

Table 1. Properties of the used LYSO detectors, including the crystal type monolithic ('mono') or pixellated ('pixel'), the dimensions (width \times height \times length) and the used lightguide, asymmetric ('asy') or symmetric ('sym').

A cubic PMMA target ($50 \times 50 \times 50 \text{ mm}^3$) was mounted on a translation table. Longitudinal prompt gamma ray profiles have been obtained by a scan of the target in front of the detectors. The detector signals were coupled to standard NIM electronics and data were registered via a VME data acquisition system. For every detector an ADC information is available, whereas only one time information from a TAC (time to amplitude converter) was provided. The start signal for the TAC came from the logic-or of the five LYSO detectors after passing constant fraction discriminators,

whereas the HF-structure of the accelerator (one bunch of 1 ns every 80 ns) served as stop. For a normalization to the incident ion flux, a NaI detector was installed at 1050 mm from the target for the registration of secondary radiation from the primary beam. This detector was placed underneath the target table at 90° with respect to the beam direction. The count rate of the NaI detector was checked to be independent of the target position. It has been calibrated via a Faraday cup. Energy calibration of all detector modules has been performed with radioactive sources.

2.2 Data analysis

For the five LYSO detectors only a single TAC had been available to give the time-of-flight (TOF) information between a start produced by an event in a detector module and the stop from the (delayed) accelerator-HF. This time information needs then to be assigned to the individual detectors in the offline analysis. For each module a software threshold (300-400 keV) is defined which corresponds to the associated hardware discriminator threshold. In order to avoid ambiguities in the assignment of the TAC information, only events with multiplicity 1 have been taken into account in a first analysis step. With this restriction only one module has an ADC entry above its software threshold and the entries of all other modules are below their respective thresholds. Fig. 3 shows the energy versus TOF spectra under these conditions for the five LYSO detectors. The spectra reveal a horizontal band below 1 MeV which can be attributed to the internal radioactivity of the LYSO detectors (β^- -decay of ^{176}Lu with end point energy 596 keV, followed by a cascade of γ -rays) and to 511 keV lines. The (close-to) vertical bands at $t \approx 25$ ns contain the prompt-gamma rays. This part is mostly pronounced for LYSO 3 and LYSO 5 as for the present target position the Bragg-peak is close to the field of view of these two detector modules. At this particular position, the beam path in the PMMA block is not in the field of view of LYSO 1 and hardly for LYSO 2. The absolute position of the prompt-gamma band depends on cable lengths and individual photomultiplier transit times, only and is not relevant for the further analysis. Besides the prompt-gammas, also neutrons are registered, they can be identified via their larger TOF values. As neutrons can traverse the collimator or produce neutron-induced secondary gamma rays, they do not carry information about the vertex of their production and therefore only contribute to background. For a selection of the relevant events, energy and TOF selections as described in [10, 13], are applied.

The red line in Figure 4 shows the TOF spectra of LYSO 3 for a target position which is close to the Bragg peak for this detector. A timing window (here with a width of 3.6 ns) is selected around the prompt peak. The widths of the prompt windows have been adapted for the individual LYSOs and their positions respect the change of TOF at different target positions. In order to account for background in these prompt regions, reference data have been taken at two positions, one before the target entrance, and the other after the Bragg peak. The blue line in Figure 4 represents the mean spectrum of these two measurements after applying a scaling factor (see [22]). Finally, the events remaining in the prompt region, after subtracting the background, are integrated. Information from the calibrated NaI detector is used for a normalization to the fluence of incident ions.

A further selection of relevant events in the data sample is performed via cuts in the energy regime. Above 1 MeV the events attributed to the internal radioactivity of LYSO are sufficiently suppressed. With the present setup the number of events for which a photon has undergone scattering in a neighboring detector module could not be quantified due to the use of a single TAC, only. The signature from the ADC entries is not sufficient for this purpose, as these signals comprise also random events

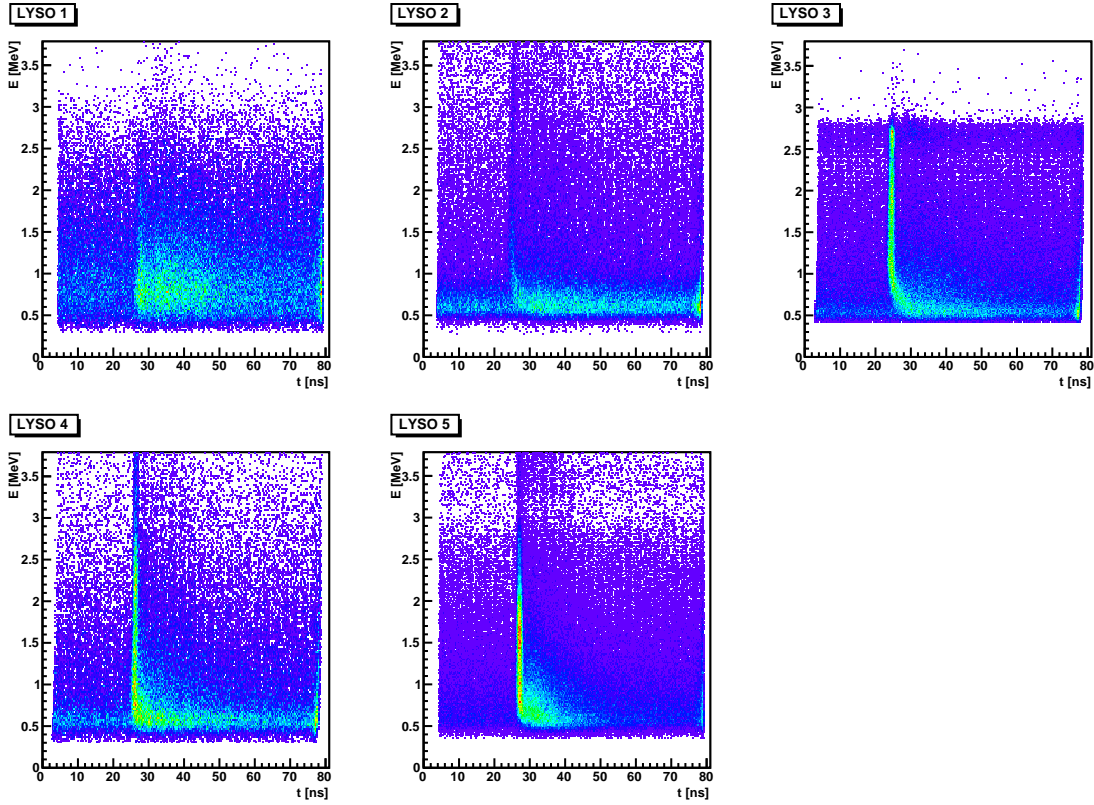


Figure 3. Energy versus TOF spectra for the five LYSO detectors under the condition of multiplicity 1. The origin of time (horizontal axis) is arbitrary.

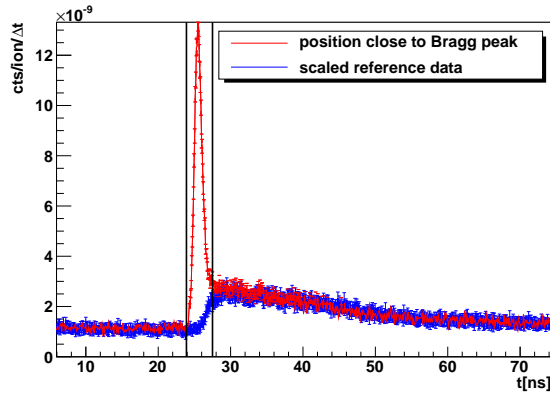


Figure 4. TOF spectrum for LYSO 2 for a position close to the Bragg peak (red line) and a scaled mean spectrum (blue line) from two reference points, one before the target, and one after the Bragg peak. The vertical lines indicate the prompt region. These spectra contain only events with energies above 1 MeV.

which arrive during the ADC gate (4-5 μ s). A dedicated experiment has therefore been performed at GSI, which will be described in section 3.

2.3 Results

With the multi-slit multi-detector configuration data have been taken at 24 different target positions in order to scan longitudinal prompt-gamma profiles (GANIL 75 MeV/u ions). In Figure 5 (left) the registered counts per incident ion are plotted as a function of the target position. For this figure

no TOF or energy selection has been applied. It is obvious that no information about the ion range can be extracted from this plot.

In the right part of this figure, a 400 keV energy threshold has been applied and TOF information

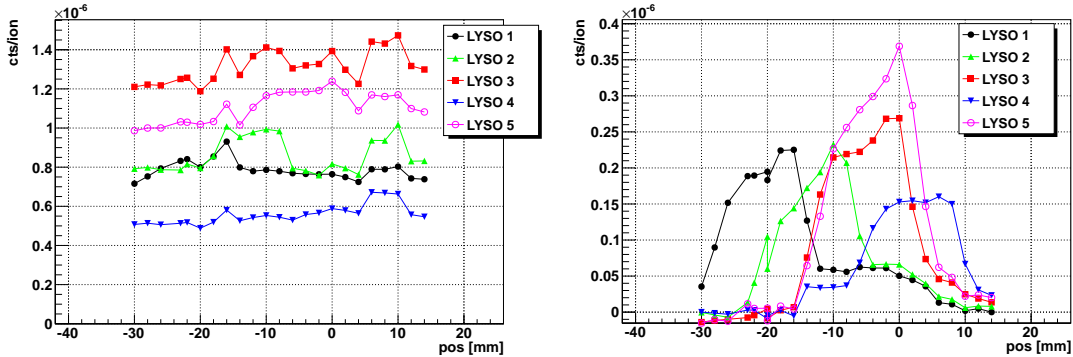


Figure 5. Longitudinal prompt gamma ray profiles, without any TOF and energy selection (left) and with a 400 keV energy threshold, including TOF information and after background subtraction (right).

has been included. Furthermore, background has been subtracted, as described in the previous section. In this plot the increase of count rate at the target entrance and the fall-off in the Bragg-peak region can be identified. For LYSO 1 and LYSO 2 another bump after the Bragg peak, around 0 mm, appears. These events come either from Compton scattering of neighboring detector modules or from an inappropriate assignment of the TAC information to the corresponding detector. With an increase of the threshold to 1 MeV and a restriction to multiplicity 1, this fraction can be minimized. The results under these conditions are shown in the left part of Figure 6.

For a better comparison of the profiles from the individual detectors, the detector positions have been taken into account and the horizontal axes have been shifted accordingly (Figure 6 right part). The vertical blue lines represent the positions of the target entrance and the range of $75 \text{ MeV/u } ^{13}\text{C}$ ions in PMMA, respectively. Although the count rates are not the same due to different detector geometries (see Table 1), the target entrance and the fall-off is revealed at positions which are con-

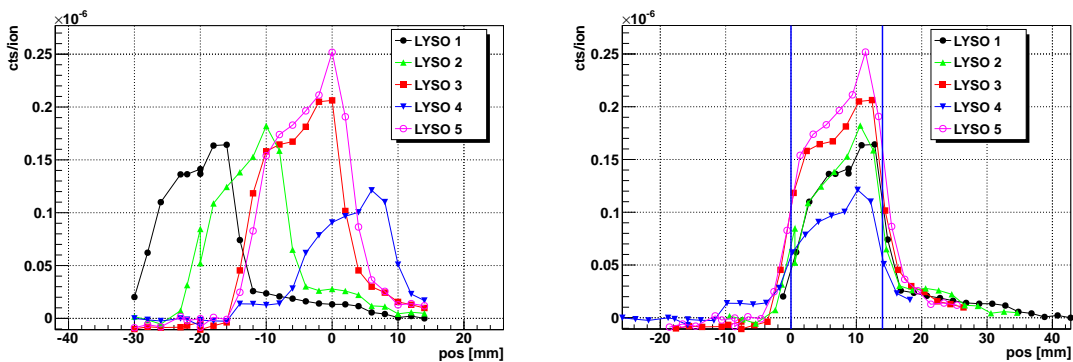


Figure 6. Left: Longitudinal prompt-gamma ray profiles with TOF selection, a 1 MeV energy threshold and under the condition of multiplicity 1. Right: the detector positions have been taken into account and the horizontal axes have been shifted accordingly, for a better comparison of the results. The vertical blue lines represent the target entrance and the range of ^{13}C ions, respectively.

sistent with the theoretical values. For a quantitative investigation of the range retrieval precision as a function of the available statistics see Ref. [21].

3. Collimator test experiment at GSI

3.1 Experimental setup

For an investigation of the scattering between detectors, as well as the influence of different collimator configurations and shieldings, a dedicated experiment has been performed with 200 MeV/u ^{12}C -ions at GSI (Darmstadt, Germany). A top-view of the complete setup is displayed in Fig. 7. The carbon ions passed a beam tagging hodoscope, consisting of an array of orthogonal scintillating fibers, which provided a time and position information. As target served a 200 mm long PMMA cylinder with a diameter of 150 mm. Produced secondary radiation was registered with LYSO detectors behind a collimator, or with a LaBr_3 detector (diameter: 25.4 mm, length: 50.8 mm) behind shielding material, respectively. LYSO 2-4 (following the labeling of Table 1) were placed behind

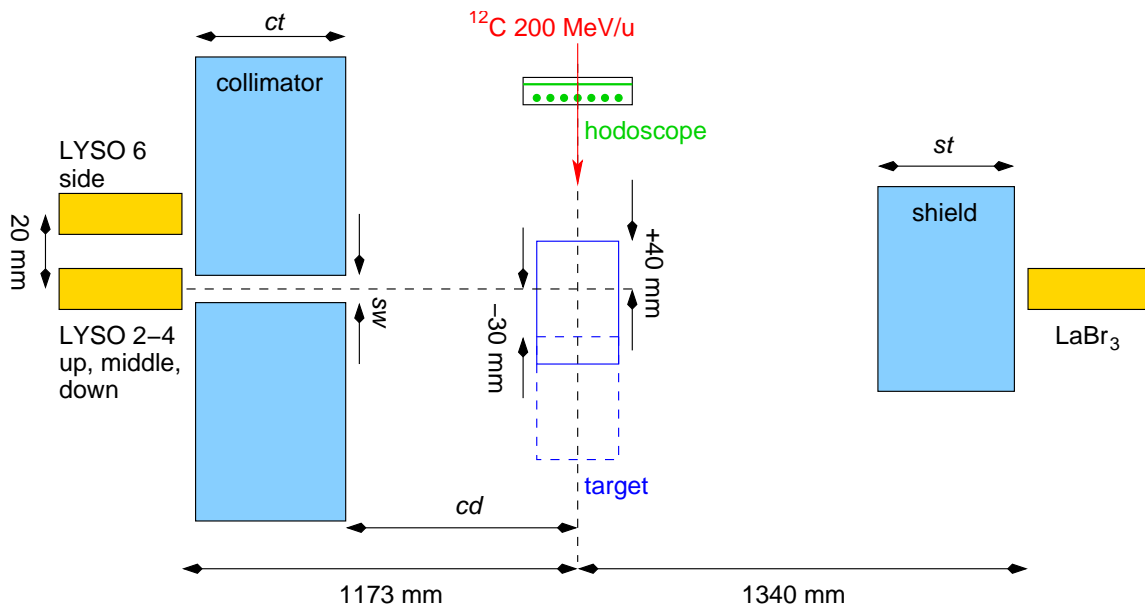


Figure 7. Setup for the investigation of inter-detector scattering and the influence of different collimator configurations and shieldings with 200 MeV/u ^{12}C -ions at GSI. Figure is not to scale.

the slit of the collimator, whereas LYSO 6 had no direct view to the target (see Fig. 8 for a side-view of the detector arrangement behind the collimator). The used detector modules are mainly the same as for the previously described experiment at GANIL. The dimensions are given in Table 1. The detector signals were connected to standard NIM electronics, and data were recorded with a VME data acquisition system. For each detector an ADC and TDC information is available. The delayed signal from the beam tagging hodoscope served as time reference for the TDC (stop signal).

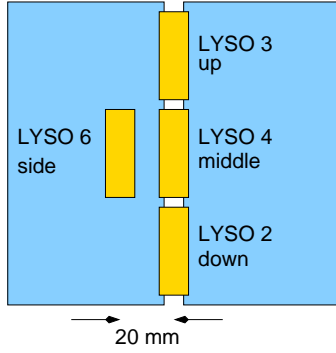


Figure 8. Arrangement of the LYSO detectors behind the collimator for the inter-detector scattering experiment.

configuration	material	distance (cd [mm])	sw [mm]	ct [mm]
0	Pb	far (1073)	4	100
1	Pb	far (1123)	4	50
2	W	far (1073)	4	100
3	W	far (1123)	4	50
4	Pb	close (760)	4	100
5	Pb	close (760)	8	100

Table 2. Different collimator configurations comprising a variation of the material, the collimator distance cd , the slit width sw , and the collimator thickness ct .

Different configurations have been tested, where the collimator material, the collimator distance cd , the slit width sw and the collimator thickness ct have been varied, whereas the distance between the target and the LYSO detectors was kept fixed at 1173 mm. Two major configurations have been realized, one with the collimator 'far' from the target, next to the detectors, and another with the collimator more 'close' to the target. An overview of the parameters for the different collimator configurations is given in Table 2. The test with different shielding materials (W and Pb) and thicknesses st (between 0 and 200 mm) was performed at a fixed distance (1340 mm) between the target and the LaBr₃ detector.

3.2 Data analysis

At this experiment each detector element has been equipped with a TDC in order to determine the number of events which have been scattered from another detector module, via their timing signature.

In a first analysis step, energy versus TOF spectra of LYSO 2-4, the three detectors behind the slit of the collimator, have been produced (Figure 9). The horizontal band in the spectra is due to the internal radioactivity of LYSO. The vertical band can be attributed to prompt gamma rays which are generated in the target and are passing the slit of the collimator. The vertical structures which appear in the upper and middle LYSO more than 20 ns before the prompt band can be attributed to beam diagnostic elements upstream to the target area. For a selection of the relevant events, an energy threshold of 1.1 MeV has been applied and prompt windows in the time domain have been defined as indicated by the red lines in the figure.

As LYSO 6 has no direct view to the target, it is only sensitive to scattered events from LYSO 2-4

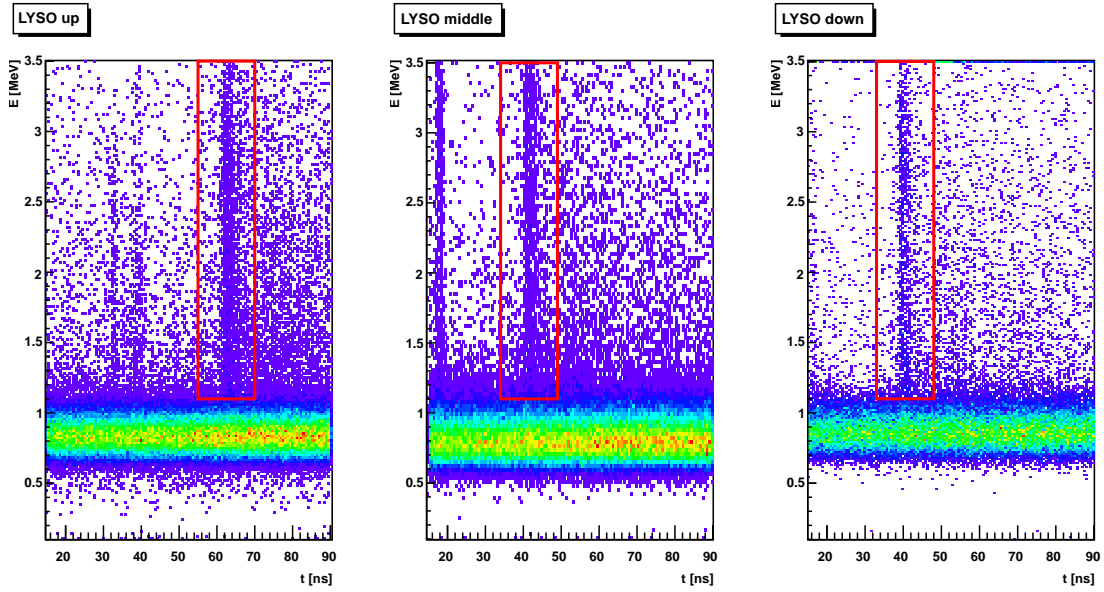


Figure 9. Energy versus TOF spectra for the three LYSO detectors behind the collimator slit. The red lines indicate the regions of selected prompt gamma ray events. The origin of the time scale is arbitrary.

or to background. For a determination of the number of scattered events, the time difference between this LYSO at the side and one of the other three LYSOs is calculated in a second analysis step. If photon scattering appears between LYSO 2-4 and LYSO 6 this time difference has a fixed value which is only determined by cable lengths and transition times of the electronics modules. For background events in LYSO 6 there would be no such time correlation with the other detector modules. For a restriction to prompt-gamma rays, the time difference t_{diff} has only been calculated for events inside the red regions of Figure 9. Furthermore, an energy threshold of 1.1 MeV has also been applied for LYSO 6. The results are given in Figure 10. The time distributions reveal sharp

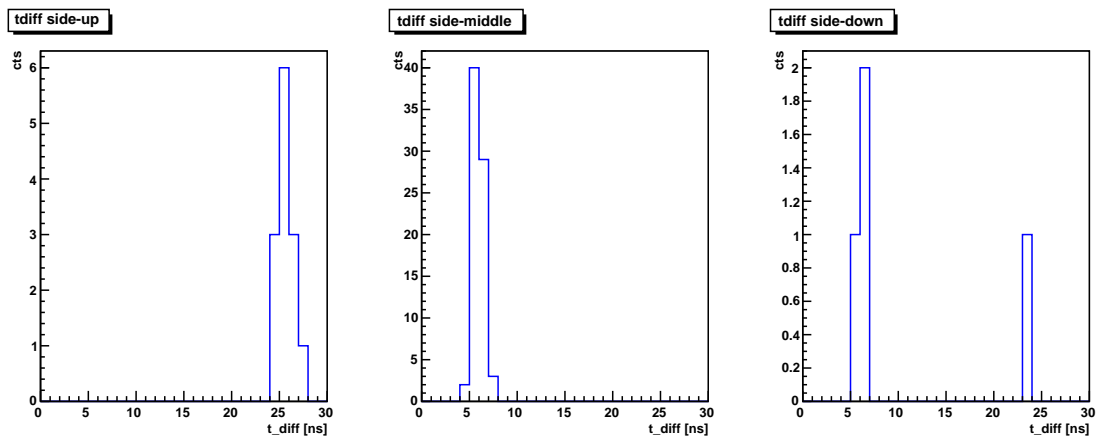


Figure 10. Time differences of the detector at the side (LYSO 6) to the three other detectors (up, middle, down).

peaks with a negligible number of random events, only. The number of entries in these spectra can therefore directly be attributed to scattered prompt-gamma events with origin LYSO 2-4 with a maximum for LYSO 4 that is set aside (cf. Fig. 8).

With the same experimental setup the influence of different collimator configurations to the contrast in prompt gamma ray profiles has been investigated. Due to time limitations data have been taken for each configuration at two target positions, only. One at -30 mm before the target and the other at +40 mm inside the target (see Fig. 7). The corresponding TOF spectra of the three

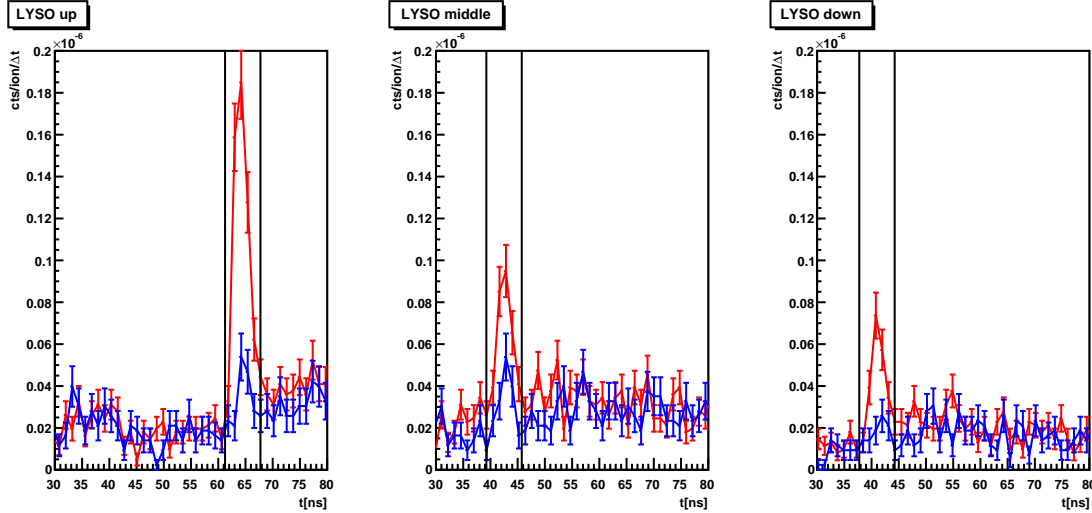


Figure 11. TOF spectra of the three LYSO detectors behind the collimator slit for configuration 0 (Table 2). The red (blue) lines represent a point with a field of view of the ion range inside (before) the target, respectively.

detectors behind the collimator slit (configuration 0, see Table 2) are given in Fig. 11, where the two target positions are represented by the blue and red lines, respectively. The number of events are obtained via integration in the prompt region indicated by the vertical lines in the figure. At the configuration 0 (lead collimator with a thickness of 100 mm) the blue spectra reveal also a prompt peak, i.e. prompt gamma rays are not completely absorbed by the collimator material.

For an investigation of shielding properties and transmission of prompt gamma rays by different materials, the LaBr_3 detector has been placed behind lead or tungsten layers with various thicknesses, respectively (see Fig. 7). Figure 12 shows the TOF spectra obtained from the LaBr_3 without shielding (red line) and with 50 mm (blue line) and 100 mm (black line) thick lead bricks in front of the detector, respectively. Furthermore, results from Geant4-simulations [23] (version 9.6.p02) are also given for the configuration with 100 mm lead shielding. For all the simulations in this article the reference physics list (QGSP_BIC_HP3), which involves the binary light ion cascade model, has been applied.

3.3 Results

The results from the measurement with a variation of shielding materials and thicknesses is given

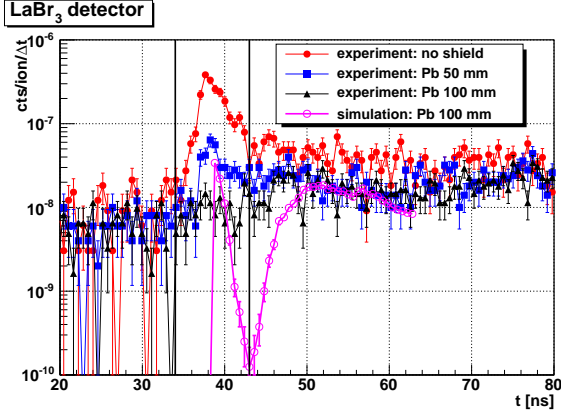


Figure 12. Experimental TOF spectra from the LaBr₃ detector without shielding (red line) and with 50 mm and 100 mm thick lead layers, respectively. For comparison simulated data is also shown for the 100 mm lead shielding.

in Fig. 13. As a measure of the prompt gamma rays which can pass through the shielding, count rates of the LaBr₃ detector have been integrated in time windows around the prompt gamma peak (Fig. 12). For the points without shielding (thickness 0) the simulated prompt-gamma production overshoots the measured one by approximately a factor 2. This effect has already been reported in the literature [24]. The discrepancy can be reduced via the use of the Quantum Molecular Dynamics (QMD) model and a tuning of the free parameters therein [25]. As for the present comparison with experiment the absolute prompt-gamma rate is not of utmost importance, this approach has not been followed here.

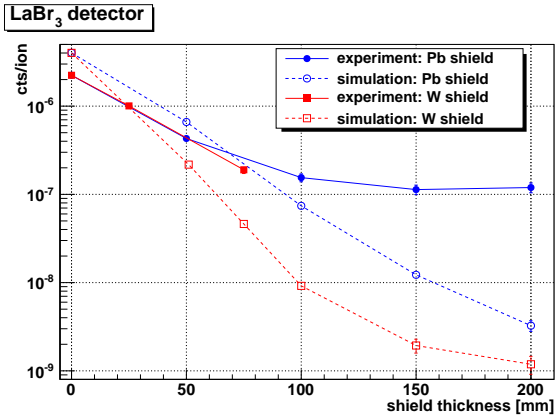


Figure 13. Integrated count rates of the LaBr₃ detector behind lead and tungsten shielding with various thicknesses in comparison with Geant4 simulations.

Both, experimental and simulated data reveal a linear behavior in the semi-logarithmic plot of Figure 13. The experimental data with the lead shielding indicate saturation effects already at a shielding thickness of 100 mm, whereas the simulated data continue to decrease with increasing shielding. The experimental TOF spectrum in Figure 12 with a 100 mm shielding does not reveal a prompt-gamma peak anymore. The integral is therefore dominated by random events. For the simulation, a perfect timing resolution has been assumed for the LaBr₃ detector, furthermore the surrounding experimental area has not been modeled. This is the reason why in the simulated data at a shielding thickness of 100 mm the prompt-gamma peak can clearly be identified and no random coincidences appear before this peak.

Regarding the shielding properties of lead and tungsten, the latter is more efficient due to its density, which is a factor 1.6 larger compared to lead. This difference in the shielding properties is

more clearly revealed in the simulations, than in the experimental data.

In a multi-slit multi-detector setup with the intended purpose of measuring longitudinal prompt-gamma profiles, inter-detector scattering of prompt-gamma rays would lead to a dilution of position information, as for the reconstruction of the profiles it is assumed that the photons passed the corresponding collimator slit in front of the detector. For scattered events this assumption is not valid anymore. The amount of this inter-detector scattering has been determined at a dedicated experiment at GSI with three LYSO detectors behind the collimator slit in coincidence with one detector at the side, without a direct view to the target (see Fig 8). The results are summarized in Table 3.

	LYSO 3 (up)	LYSO 4 (middle)	LYSO 2 (down)
scattered	13	74	4
total	3633	3217	2102
ratio	0.4%	2.3%	0.2%
ratio (Geant4)	0.6%	3.8%	0.2%

Table 3. Scattered and total number of prompt-gamma ray events for the three LYSO detectors behind the collimator slit. The number of scattered events (in coincidence with LYSO 6 positioned as in Figure 8) were extracted from Figure 10, whereas the total numbers were accumulated inside the regions indicated by the red lines of Figure 9.

The number of scattered prompt-gamma ray events which have been registered with LYSO 6 were extracted from Fig. 10. The total number of prompt-gamma rays in LYSO 2-4 were accumulated inside the regions indicated by the red lines of Figure 9. Most of the scattered events have their origin in the middle detector (LYSO 4) which is next to LYSO 6 (Fig. 8). However, the fraction is less than 3%, which corresponds to a minor dilution of the position information, only. The slightly higher values in the simulated data can be ascribed to the use of the Binary Cascade (BIC) model inside Geant4.

For a further investigation of the inter-detector scattering a simulated configuration with five extra LYSO detectors (L6_1-L6_5) next to LYSO 6 has been realized (Fig. 14 left). The right part of this

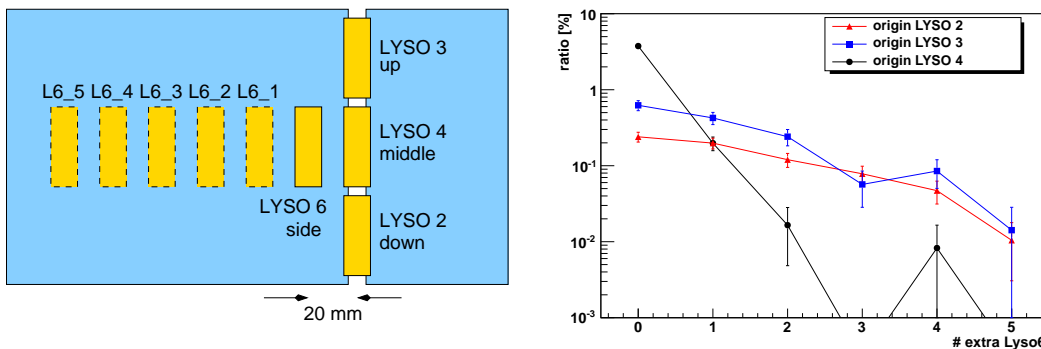


Figure 14. Left: Simulated configuration with five additional LYSO detectors (L6_1-L6_5) for a further investigation of inter-detector scattering. Right: Results from the simulation. Ratio of detected events in the extra LYSO detectors to the number of events in their origin detector.

figure gives the ratio of events detected in these additional detectors to the number of events in their origin detector (LYSO 2-LYSO 4). The points at zero correspond to LYSO 6 (cf. Table 3). The points with origin LYSO 4 indicate that scattering from a detector which is not the next neighbor is suppressed by at least an order of magnitude and can therefore be neglected.

The results from the measurements with different collimator configurations are displayed in Figure 15. The integrated signals (Fig. 11) of the three LYSO detectors behind the collimator slit are shown for each of the six different collimator configurations (Table 2). Data have been taken

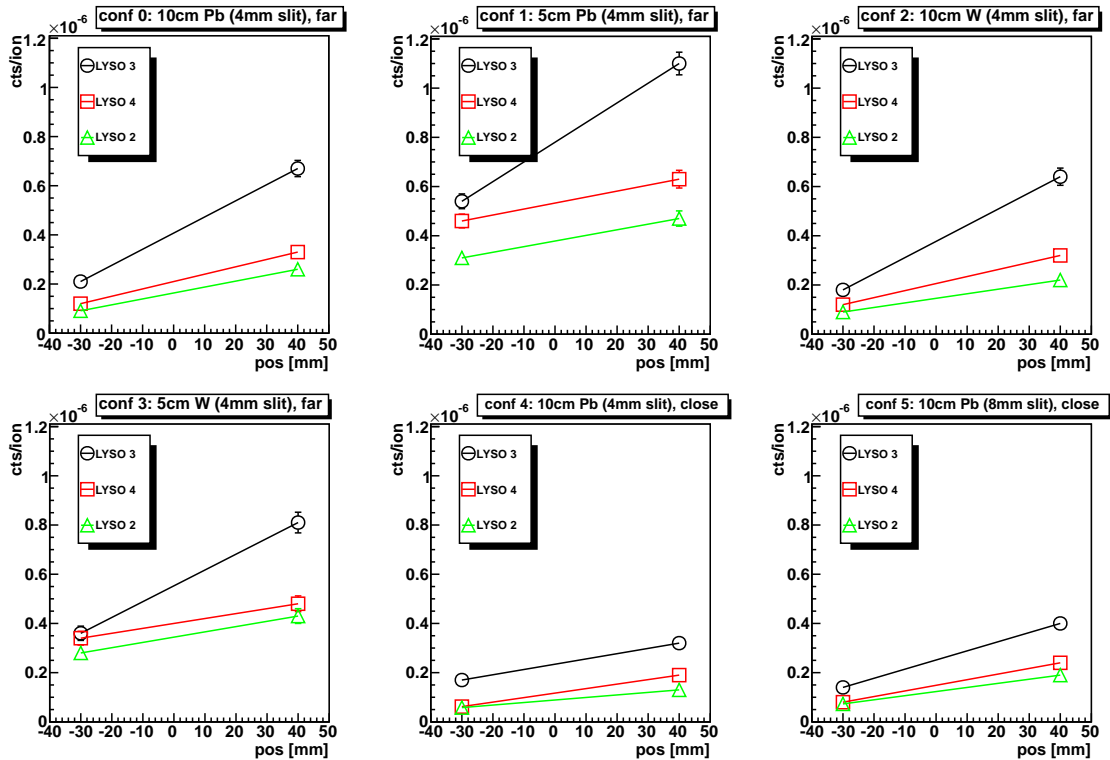


Figure 15. Integrated signals of the three LYSO detectors behind the collimator slit at the target positions -30 mm and +40 mm for the six different collimator configurations (Table 2).

at the target positions -30 mm and +40 mm, respectively. The differences of the integrated count rates at these two positions are displayed for the six different collimator configurations in the upper part of Figure 16. This contrast is more pronounced for the configurations with the collimator 'far' from the target (Nr. 0 to 3) as here the field-of-view is larger than at a 'close' configuration with the same slit width s_w . For a better interpretation of the results from the three LYSO detectors the arithmetic mean is also shown in the figure (blue points).

The lower part of Figure 16 shows the ratio of the contrast to the background which corresponds to the count rate at the point before the target (-30 mm). This ratio is reduced for the two configurations with thinner collimators (Nr.1 and 3) which do not provide complete absorption of the prompt gamma rays. The results from configuration 5 (collimator 'close', 8 mm slit width) are compatible

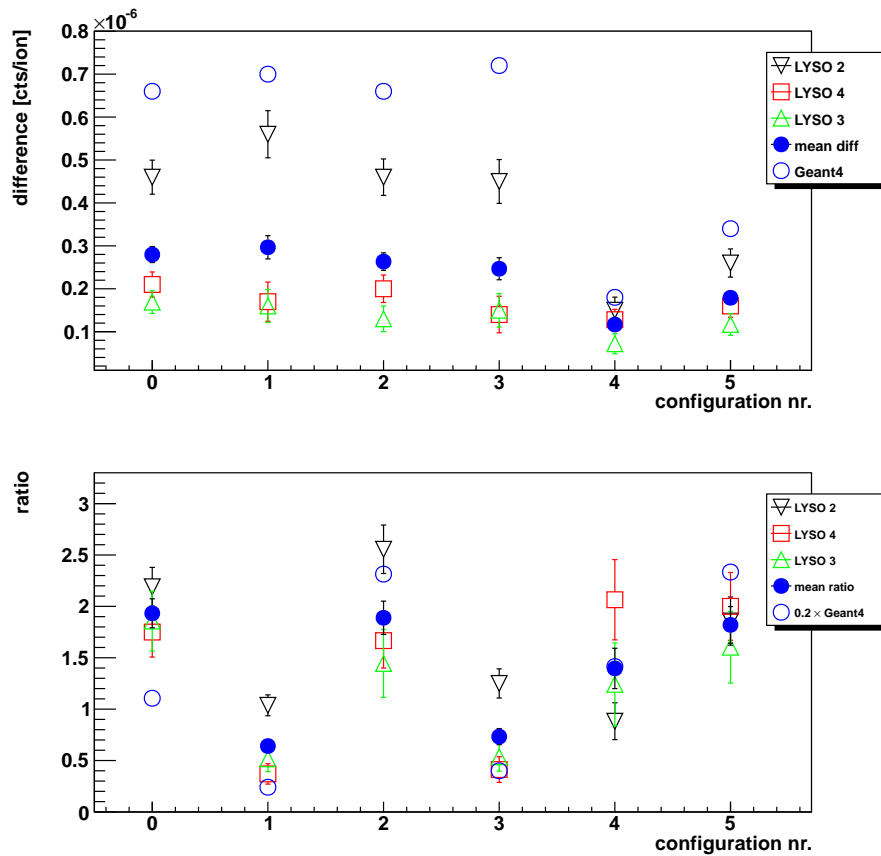


Figure 16. Up: Difference of the integrated count rates at the two positions (-30 mm and +40 mm) for the six different collimator configurations as a measure for the contrast. Down: Ratio of the contrast to background (point at -30 mm) for the different configurations. For a better interpretation of the results the arithmetic mean from the three LYSO detectors has been calculated (blue points). Also shown are the results of the arithmetic mean from the simulations (open circles). For a better comparison with experiment, a factor 0.2 has been applied for the ratios (lower plot).

with the ones from the 'far' configuration and thick collimators (Nr. 0 and 2).

In this figure also the results from the Geant4 simulations for the arithmetic mean of the three LYSO detectors are displayed (open circles). As mentioned above, more prompt gammas are produced and less background appears in the simulations, compared to experimental data. Nevertheless, even if absolute values cannot be reproduced, the results from Geant4 nicely follow the trend from the experiment for the different configurations (Fig. 16 up). For the ratio, displayed in the lower part of the figure, a factor 0.2 has been applied to the simulations, for a better comparison with experiment. Also here, the simulations reflect the tendency of the data for the different collimator configurations.

4. Conclusions

As an intermediate step towards a clinical prototype of a collimated camera for online ion range

monitoring during hadrontherapy via the detection of prompt gamma rays, measurements have been performed with a multi-slit multi-detector configuration at a 75 MeV/u ^{13}C beam impinging on a PMMA target. It has been shown that a selection of TOF and energy is necessary before information about the ion range can be extracted from the measurement of count rates at different target positions. The results for the five individual LYSO detector modules are in agreement with theoretical expectations. Prompt-gamma rays which undergo scattering in neighboring detector modules would dilute the information about the origin of the gamma rays and would therefore reduce the contrast. The fraction of these events has been determined in a separate experiment with 200 MeV/u ^{12}C ions. It has been demonstrated that this part plays a minor role with a fraction of less than 3%, only. Different collimator configurations have been tested and shielding properties of lead and tungsten have been measured. The results from Geant4 simulations are in agreement with experimental data, even if absolute prompt gamma production rates are overestimated by the simulations, the relative performance of the different collimator configurations could be reproduced. This confirms the use of Geant4 for a further optimization of the collimator dimensions. Besides the signal contrast these simulations also take into account the range retrieval precision of the incident ions. The results from this collimator optimization will be subject of a forthcoming article [26].

Acknowledgments

This research project has been partly supported by the Regional Program for Research in Hadrontherapy (PRRH, under CPER 2007-13 funding), the ENVISION European project (grant agreement nr. 241851) and ENTERVISION (grant agreement nr. 264552), the ANR Gamhadron project (ANR-09-BLAN-0106). This work was performed within the framework of the LABEX PRIMES (ANR-11-LABX-0063).

References

- [1] G. Shakirin, H. Braess, F. Fiedler, D. Kunath, K. Laube, K. Parodi, M. Priegnitz, W. Enghardt, Implementation and workflow for PET monitoring of therapeutic ion irradiation: a comparison of in-beam, in-room, and off-line techniques, *Phys. Med. Biol.* 56 (5) (2011) 1281.
URL <http://stacks.iop.org/0031-9155/56/i=5/a=004>
- [2] W. Enghardt, P. Crespo, F. Fiedler, R. Hinz, K. Parodi, J. Pawelke, F. Pönisch, Charged hadron tumour therapy monitoring by means of PET, *Nucl. Instr. Methods A* 525 (1-2) (2004) 284 – 288, proceedings of the International Conference on Imaging Techniques in Subatomic Physics, Astrophysics, Medicine, Biology and Industry.
URL <http://www.sciencedirect.com/science/article/pii/S0168900204004218>
- [3] T. Nishio, T. Ogino, K. Nomura, H. Uchida, Dose-volume delivery guided proton therapy using beam on-line PET system, *Med. Phys.* 33 (2006) 4190.
- [4] U. Amaldi, W. Hajdas, S. Iliescu, N. Malakhov, J. Samarati, F. Sauli, D. Watts, Advanced quality assurance for CNAO, *Nucl. Instr. Methods A* 617 (1-3) (2010) 248 – 249.
URL <http://www.sciencedirect.com/science/article/pii/S0168900209013424>

- [5] P. Henriquet, E. Testa, M. Chevallier, D. Dauvergne, G. Dedes, N. Freud, J. Krimmer, J. M. Létang, C. Ray, M.-H. Richard, F. Sauli, Interaction vertex imaging (IVI) for carbon ion therapy monitoring: a feasibility study, *Phys. Med. Biol.* 57 (14) (2012) 4655.
URL <http://stacks.iop.org/0031-9155/57/i=14/a=4655>
- [6] C. Agodi, G. Battistoni, F. Bellini, G. A. P. Cirrone, F. Collamati, G. Cuttone, E. D. Lucia, M. D. Napoli, A. D. Domenico, R. Faccini, F. Ferroni, S. Fiore, P. Gauzzi, E. Iarocci, M. Marafini, I. Mattei, S. Muraro, A. Paoloni, V. Patera, L. Piersanti, F. Romano, A. Sarti, A. Sciubba, E. Vitale, C. Voena, Charged particle's flux measurement from PMMA irradiated by 80 MeV/u carbon ion beam, *Phys. Med. Biol.* 57 (18) (2012) 5667.
URL <http://stacks.iop.org/0031-9155/57/i=18/a=5667>
- [7] K. Gwosch, B. Hartmann, J. Jakubek, C. Granja, P. Soukup, O. Jäkel, M. Martišíková, Non-invasive monitoring of therapeutic carbon ion beams in a homogeneous phantom by tracking of secondary ions, *Phys. Med. Biol.* 58 (11) (2013) 3755.
URL <http://stacks.iop.org/0031-9155/58/i=11/a=3755>
- [8] C.-H. Min, C. H. Kim, M.-Y. Youn, J.-W. Kim, Prompt gamma measurements for locating the dose falloff region in the proton therapy, *Appl. Phys. Lett.* 89 (18) (2006) 183517.
URL <http://link.aip.org/link/?APL/89/183517/1>
- [9] C. H. Kim, C. H. Min, K. S. Seo, J.-W. Kim, Simulation studies on the correlation of distal dose falloff of a 70-MeV proton beam with a prompt gamma distribution, *Journal of the Korean Physical Society* 50 (5) (2007) 1510–1513.
- [10] E. Testa, M. Bajard, M. Chevallier, D. Dauvergne, F. L. Foulher, N. Freud, J.-M. Letang, J.-C. Poizat, C. Ray, M. Testa, Monitoring the Bragg peak location of 73 MeV/u carbon ions by means of prompt gamma-ray measurements, *Appl. Phys. Lett.* 93 (9) (2008) 093506.
URL <http://link.aip.org/link/?APL/93/093506/1>
- [11] V. Bom, L. Joulaeizadeh, F. Beekman, Real-time prompt gamma monitoring in spot-scanning proton therapy using imaging through a knife-edge-shaped slit, *Phys. Med. Biol.* 57 (2) (2012) 297.
URL <http://stacks.iop.org/0031-9155/57/i=2/a=297>
- [12] J. Smeets, F. Roellinghoff, D. Prieels, F. Stichelbaut, A. Benilov, P. Busca, C. Fiorini, R. Peloso, M. Basilavecchia, T. Frizzi, J. C. Dehaes, A. Dubus, Prompt gamma imaging with a slit camera for real-time range control in proton therapy, *Phys. Med. Biol.* 57 (11) (2012) 3371.
URL <http://stacks.iop.org/0031-9155/57/i=11/a=3371>
- [13] M. Testa, M. Bajard, M. Chevallier, D. Dauvergne, N. Freud, P. Henriquet, S. Karkar, F. Le Foulher, J. Létang, R. Plescak, C. Ray, M.-H. Richard, D. Schardt, E. Testa, Real-time monitoring of the Bragg-peak position in ion therapy by means of single photon detection, *Rad. Env. Biophys.* 49 (2010) 337–343, 10.1007/s00411-010-0276-2.
URL <http://dx.doi.org/10.1007/s00411-010-0276-2>
- [14] C. H. Min, H. R. Lee, C. H. Kim, S. B. Lee, Development of array-type prompt gamma measurement system for in vivo range verification in proton therapy, *Med. Phys.* 39 (4) (2012) 2100–2107.
URL <http://link.aip.org/link/?MPH/39/2100/1>
- [15] S. W. Peterson, D. Robertson, J. Polf, Optimizing a three-stage Compton camera for measuring prompt gamma rays emitted during proton radiotherapy, *Phys. Med. Biol.* 55 (22) (2010) 6841.
URL <http://stacks.iop.org/0031-9155/55/i=22/a=015>

- [16] H. Seo, J. H. Park, A. Ushakov, C. H. Kim, J. K. Kim, J. H. Lee, C. S. Lee, J. S. Lee, Experimental performance of double-scattering Compton camera with anthropomorphic phantom, *JINST* 6 (01) (2011) C01024.
URL <http://stacks.iop.org/1748-0221/6/i=01/a=C01024>
- [17] M.-H. Richard, D. Dahoumane, M. and Dauvergne, M. De Rydt, G. Dedes, N. Freud, J. Krimmer, J. Létang, X. Lojaco, V. Maxim, G. Montarou, C. Ray, F. Roellinghoff, E. Testa, A. Walenta, Design study of the absorber detector of a Compton camera for on-line control in ion beam therapy, *IEEE Trans. Nucl. Sci.* 59 (5) (2012) 1850–1855.
- [18] S. Kurosawa, H. Kubo, K. Ueno, S. Kabuki, S. Iwaki, M. Takahashi, K. Taniue, N. Higashi, K. Miuchi, T. Tanimori, D. Kim, J. Kim, Prompt gamma detection for range verification in proton therapy, *Current Applied Physics* 12 (2) (2012) 364 – 368.
URL
<http://www.sciencedirect.com/science/article/pii/S1567173911004123>
- [19] T. Kormoll, F. Fiedler, S. Schöne, J. Wüstemann, K. Zuber, W. Enghardt, A Compton imager for in-vivo dosimetry of proton beams - design study, *Nucl. Instr. Methods A* 626-627 (0) (2011) 114 – 119.
URL
<http://www.sciencedirect.com/science/article/pii/S0168900210022709>
- [20] G. Llosá, J. Cabello, S. Callier, J. Gillam, C. Lacasta, M. Rafecas, L. Raux, C. Solaz, V. Stankova, C. de La Taille, M. Trovato, J. Barrio, First Compton telescope prototype based on continuous LaBr₃-SiPM detectors, *Nucl. Instr. Methods A* 718 (0) (2013) 130 – 133.
URL
<http://www.sciencedirect.com/science/article/pii/S0168900212009771>
- [21] F. Roellinghoff, A. Benilov, D. Dauvergne, G. Dedes, N. Freud, G. Janssens, J. Krimmer, J. M. Létang, M. Pinto, D. Prieels, C. Ray, J. Smeets, F. Stichelbaut, E. Testa, Real-time proton beam range monitoring by means of prompt-gamma detection with a collimated camera, *Physics in Medicine and Biology* 59 (5) (2014) 1327.
URL <http://stacks.iop.org/0031-9155/59/i=5/a=1327>
- [22] M. Pinto, et al., submitted to *Phys. Med. Biol.*
- [23] S. Agostinelli, J. Allison, K. Amako, J. Apostolakis, H. Araujo, P. Arce, M. Asai, D. Axen, S. Banerjee, G. Barrand, F. Behner, L. Bellagamba, J. Boudreau, L. Broglia, A. Brunengo, H. Burkhardt, S. Chauvie, J. Chuma, R. Chytrcek, G. Cooperman, G. Cosmo, P. Degtyarenko, A. Dell'Acqua, G. Depaola, D. Dietrich, R. Enami, A. Feliciello, C. Ferguson, H. Fesefeldt, G. Folger, F. Foppiano, A. Forti, S. Garelli, S. Giani, R. Giannitrapani, D. Gibin, J. G. Cadenas, I. González, G. G. Abril, G. Greeniaus, W. Greiner, V. Grichine, A. Grossheim, S. Guatelli, P. Gumplinger, R. Hamatsu, K. Hashimoto, H. Hasui, A. Heikkinen, A. Howard, V. Ivanchenko, A. Johnson, F. Jones, J. Kallenbach, N. Kanaya, M. Kawabata, Y. Kawabata, M. Kawaguti, S. Kelner, P. Kent, A. Kimura, T. Kodama, R. Kokoulin, M. Kossov, H. Kurashige, E. Lamanna, T. Lampén, V. Lara, V. Lefebvre, F. Lei, M. Liendl, W. Lockman, F. Longo, S. Magni, M. Maire, E. Medernach, K. Minamimoto, P. M. de Freitas, Y. Morita, K. Murakami, M. Nagamatsu, R. Nartallo, P. Nieminen, T. Nishimura, K. Ohtsubo, M. Okamura, S. O'Neale, Y. Oohata, K. Paech, J. Perl, A. Pfeiffer, M. Pia, F. Ranjard, A. Rybin, S. Sadilov, E. D. Salvo, G. Santin, T. Sasaki, N. Savvas, Y. Sawada, S. Scherer, S. Sei, V. Sirotenko, D. Smith, N. Starkov, H. Stoecker, J. Sulkimo, M. Takahata, S. Tanaka, E. Tcherniaev, E. S. Tehrani, M. Tropeano, P. Truscott, H. Uno, L. Urban, P. Urban, M. Verderi, A. Walkden, W. Wander, H. Weber, J. Wellisch, T. Wenaus, D. Williams, D. Wright, T. Yamada,

H. Yoshida, D. Zschiesche, Geant4-a simulation toolkit, Nuclear Instruments and Methods in Physics Research Section A: Accelerators, Spectrometers, Detectors and Associated Equipment 506 (3) (2003) 250 – 303.

URL

<http://www.sciencedirect.com/science/article/pii/S0168900203013688>

- [24] F. Le Foulher, M. Bajard, M. Chevallier, D. Dauvergne, N. Freud, P. Henriquet, S. Karkar, J.-M. Letang, L. Lestand, R. Plescak, C. Ray, D. Schardt, E. Testa, M. Testa, Monte Carlo simulations of prompt-gamma emission during carbon ion irradiation, Nuclear Science, IEEE Transactions on 57 (5) (2010) 2768–2772.

URL

<http://ieeexplore.ieee.org/xpl/articleDetails.jsp?arnumber=5603703>

- [25] G. Dedes, M. Pinto, D. Dauvergne, N. Freud, J. Krimmer, J. M. Létang, C. Ray, E. Testa, Assessment and improvements of Geant4 hadronic models in the context of prompt-gamma hadrontherapy monitoring, Physics in Medicine and Biology 59 (7) (2014) 1747.

URL <http://stacks.iop.org/0031-9155/59/i=7/a=1747>

- [26] M. Pinto, et al., submitted to Phys. Med. Biol.